ADVANCED FUNCTIONAL MATERIALS
www.afm-journal.de

Alkoxy-Functionalized Thienyl-Vinylene Polymers for Field-Effect Transistors and All-Polymer Solar Cells

Hui Huang, Nanjia Zhou, Rocio Ponce Ortiz, Zhihua Chen, Stephen Loser, Shiming Zhang, Xugang Guo, Juan Casado, J. Teodomiro López Navarrete, Xinge Yu, Antonio Facchetti, and Tobin J. Marks**

π-conjugated polymers based on the electron-neutral alkoxy-functionalized thienyl-vinylene (TVTOEt) building-block co-polymerized, with either BDT (benzodithiophene) or T2 (dithiophene) donor blocks, or NDI (naphthalenediimide) as an acceptor block, are synthesized and characterized. The effect of BDT and NDI substituents (alkyl vs alkoxy or linear vs branched) on the polymer performance in organic thin film transistors (OTFTs) and all-polymer organic photovoltaic (OPV) cells is reported. Comonomer selection and backbone functionalization substantially modifies the polymer MO energies, thin film morphology, and charge transport properties, as indicated by electrochemistry, optical spectroscopy, X-ray diffraction, AFM, DFT calculations, and TFT response. When polymer P7 is used as an OPV acceptor with PTB7 as a donor, the corresponding blend yields TFTs with ambipolar mobilities of $\mu_e = 5.1 \times 10^{-3}$ cm^2 V^{-1} s^{-1} and $\mu_h = 3.9 \times 10^{-3}$ cm^2 V^{-1} s^{-1} in ambient, among the highest mobilities reported to date for all-polymer bulk heterojunction TFTs, and all-polymer solar cells with a power conversion efficiency (PCE) of 1.70%, the highest reported PCE to date for an NDI-polymer acceptor system. The stable transport characteristics in ambient and promising solar cell performance make NDI-type materials promising acceptors for all-polymer solar cell applications.

1. Introduction

In the last decade, π-conjugated polymeric materials have emerged as promising semiconductors for low-cost organic optoelectronic applications, such as organic thin-film transistors (OTFTs)[1] and photovoltaics (OPVs)[2] to cite two device categories. Planar π-conjugated building blocks represent a key target for high-performance polymeric semiconductors, since π-system planarization facilitates π-electron delocalization and charge transport.[3] Furthermore, coplanar geometries and structure rigidification can suppress rotational disorder about single bonds and lower Marcus reorganization energies, both of which enhance carrier mobility.[4] In this regard, conjugated skeletons have been rigidified into mutually fused structures by hybridizing various aromatic or heteroatom groups to promote planarity and charge transport efficiency.[5] However, achieving chemical rigidification by this means can be synthetically challenging, and may sometimes compromise cost-effectiveness and solubility. An alternative strategy is to introduce intramolecular rigidification via supramolecular interactions within the aromatic backbones. For example, weak covalent interactions, as in O···S contacts between alkoxyl groups and the S atom of thiophenes have been successfully employed to promote macromolecular planarity (**Figure 1**).[6] However, the strongly electron-donating alkoxy groups raise the π-system HOMOs[7] and thereby compromise the ambient oxidative stability of the corresponding p-channel semiconductors.[8] Furthermore, while this approach may facilitate hole or ambipolar transport, it is typically unsuitable for achieving efficient unipolar electron transport properties.[9] We recently reported a new bisthienyl-vinylene building block functionalized with alkoxyl groups at the C = C linkage and having a low HOMO energy (**TVTOEt**, Figure 1).[10] Implementing this building block with a BDT donor and an NDI acceptor moieties yields the p- and n-type conjugated polymers of structure: TVTOEt-BDTR (e.g., **P3**) and TVTOEt-NDIR (e.g., **P7**), respectively (Figure 1). More importantly, these **TVTOEt**-based n- and p-type polymers exhibit high TFT mobilities in air (n-type:

Dr. H. Huang, N. Zhou, Dr. R. P. Ortiz, S. Loser, Dr. S. Zhang, Dr. X. Guo, X. Yu, Prof. A. Facchetti, Prof. T. J. Marks
Argonne-Northwestern Solar Energy Research Center
Department of Chemistry and
the Materials Research Center
Northwestern University
2145 Sheridan Road, Evanston, IL 60208, USA
E-mail: a-facchetti@northwestern.edu; t-marks@northwestern.edu
Dr. H. Huang
College of Materials Science and Opto-Electronic Technology
University of Chinese Academy of Sciences
No.19A Yuquan Road, Beijing, 100049, China
Dr. R. P. Ortiz, Prof. J. Casado, Prof. J. T. L. Navarrete
Department of Physical Chemistry
University of Málaga
Malaga, 29071, Spain
Dr. Z. Chen, Prof. A. Facchetti
Polyera Corporation, 8045 Lamon Avenue, Skokie, IL 60077, USA

DOI: 10.1002/adfm.201303219

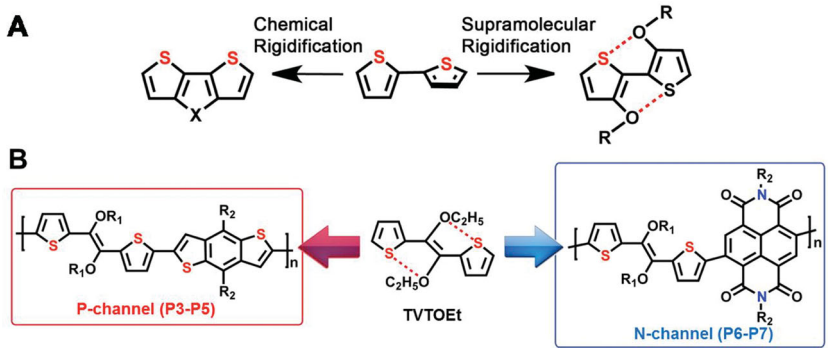

Figure 1. A) Chemical rigidification vs supramolecular rigidification and B) TVTOEt-BDTR p- and TVTOEt-NDIR n-type polymers.

0.2–0.5 cm^2 V^{-1} s^{-1}; p-type: 0.02–0.05 cm^2 V^{-1} s^{-1}), and have excellent ambient stability. However, only two types of cores and alkyl substituents were investigated. Note that polymer backbone functionalization with alkyl chains can significantly influence semiconducting properties. While linear[5c,11] or branched[12] alkyl substituents can enhance macromolecule solubility/processability, their inductive electron-donating characteristics can destabilize thiophene ring HOMO energies by as much as 0.2 eV.[13] Furthermore, intermolecular interdigitative self-assembly of alkyl side chains can assist lamellar-ordered solid state structure formation, strongly enhancing intermolecular charge transport.[14] Thus, functionalizing the same polymer backbones with modified alkyl chains can yield very different semiconducting properties and is an objective of the present study.[15]

It will also be seen here that the low-lying LUMOs, high electron mobilities, and the ambient stability of TVTOEt-NDIR-type materials offer promise as polymeric acceptors in bulk-heterojunction (BHJ) OPV cells.[16] Compared to traditional silicon solar cells, BHJ OPV active layers can be deposited on flexible substrates via scalable, low-temperature coating techniques. Recently, power conversion efficiencies (PCEs) have surpassed 5–9% for OPVs based on conjugated polymer/fullerene blends as the photoactive layer.[17] Note that the electron acceptors in these devices are typically soluble fullerenes such as (6,6)-phenyl-C_{61}-butyric methyl ester (PCBM), and these have dominated the field due to the rapid photoinduced charge transfer, good electron carrier stabilization, and high electron mobility.[1f] However, PCBM is expensive and has modest visible region optical absorption. To address this deficiency, several laboratories have investigated n-type polymers as acceptors in all-polymer solar cells, identifying several candidates.[1g,18] In such blends, both donor and acceptor materials can, in principle, exhibit large optical transition dipoles and span complementary solar spectral regions. Furthermore, the structural versatility and synthetic accessibility of conjugated polymers enables fine-tuning of each component's individual optoelectronic properties so as to optimize the optical cross-section, charge dissociation/transport efficiency, and charge collection characteristics. Nevertheless, very few effective acceptor polymers have been discovered, and the highest PCEs reported in the peer-reviewed literature for all-polymer OPVs are still currently in the 1.5–3.0% range.[19]

In this contribution, we report a new series of **TVTOEt**-based copolymers (**P1-P7**) varying in the π-co-unit (BDTR vs T2R vs NDIR) and R side chain substituents (linear alkyl vs branched alkyl vs alkoxy) (**Figure 2**). The relationship between the polymer architecture and optoelectronic device performance is characterized via studies of thin film microstructure, opto-electronic properties, and DFT quantum-chemical calculations. Due to the potential of **P7** as a polymeric OPV acceptor, the ambipolar transport properties and photovoltaic response of **P7**-based blends

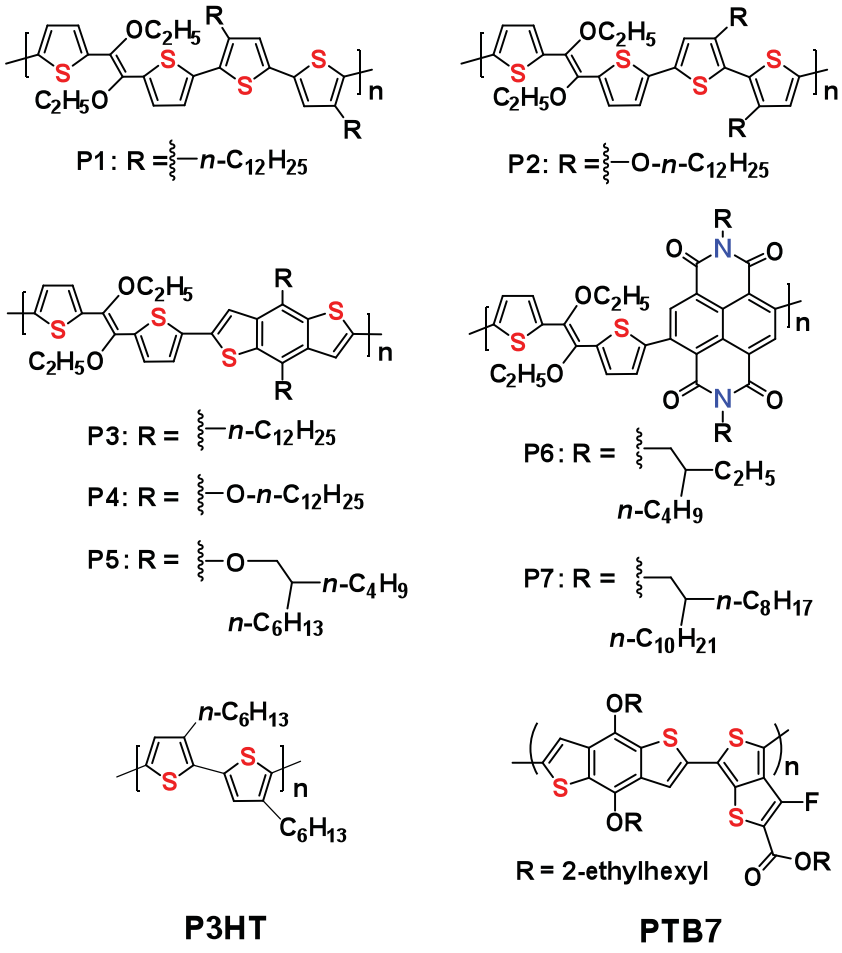

Figure 2. Structures of semiconducting polymers **P1-P7**, P3HT, and PTB7.

Table 1. Summary of thermal, optical absorption, and electrochemical properties of polymers **P1-P7**, and the corresponding estimated frontier molecular orbital energies.

Polymer	Structure	T_{TGA} [°C][a)]	$E^{red\text{-}1/2}$ [V][b)]	$E^{ox\text{-}1/2}$ [V][b)]	E_{LUMO} [eV][c)]	E_{HOMO} [eV][d)]	$\lambda_{max}^{solution}$ [nm][e)]	$\lambda_{max}^{thin\text{-}film}$ [nm] (E_g [eV])[f)]
P1	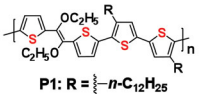 **P1: R = –*n*-$C_{12}H_{25}$**	328	–	0.85	–3.37	–5.25	494	528 (1.83)
P2	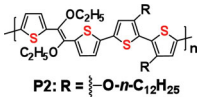 **P2: R = –O-*n*-$C_{12}H_{25}$**	293	–	0.80	–3.48	–5.20	540	577 (1.77)
P3	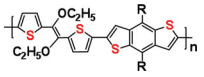 **P3: R = –*n*-$C_{12}H_{25}$**	344	–	0.82	–3.18	–5.22	520	518 (2.04)
P4		309	–	0.80	–3.26	–5.20	523	521 (1.94)
P5		303	–	0.64	–3.21	–5.28	494	492 (2.07)
P6		315	–0.30	–	–4.10	–5.64	660, 388	705, 343 (1.46)
P7		414	–0.36	–	–4.04	–5.63	744, 396	725, 399 (1.43)

[a)]5% weight loss temperature by thermogravimetric analysis under N_2; [b)]For oligomers, 0.1 M $Bu_4N^+PF_6^-$ in THF (vs SCE) at scan rate of 100 mV s^{-1}. For polymers, as thin-films, 0.1 M $Bu_4N^+PF_6^-$ in acetonitrile (vs SCE/); [c)]**P1-P5**: E_{LUMO} calculated from: $E_g = E_{LUMO} - E_{HOMO}$; **P6-P7**: estimated from equation: $E_{LUMO} = -4.40$ eV $- E_{film.}^{red-1/2}$; [d)]**P1-P5**: Estimated from equation: $E_{HOMO} = -4.40$ eV $- E_{film.}^{ox-1/2}$; **P6-P7**. E_{HOMO} calculated from: $E_g = E_{LUMO} - E_{HOMO}$; [e)]From optical absorption in *o*-DCB; [f)]The optical band gap (E_g) is caculated from hc/λ, where h is the Planck's constant, c is the speed of light, and λ is the low energy band edge wavelength of optical spectra, taking 10% of the maximum as the band edge.

with donor polymers **P3**, poly(3-hexylthiophene) (P3HT), and poly[[4,8-bis[(2-ethylhexyl)oxy]benzo[1,2-b:4,5-b′]dithiophene-2,6-diyl][3-fluoro-2-[(2-ethylhexyl)carbonyl]thieno[3,4-b]thiophenediyl]] (PTB7)[20] (Figure 2) are also investigated. It will be seen that PTB7:**P7** blends enable, under appropriate processing conditions, ambipolar transistors exhibiting comparable n-type and p-type mobilities of $\mu_e = 5.1 \times 10^{-3}$ cm^2 V^{-1} s^{-1} and $\mu_h = 3.9 \times 10^{-3}$ cm^2 V^{-1} s^{-1}, which are among the highest reported to date for bulk-heterojunction all-polymer blends.[21] Furthermore, preliminary results show that PTB7:**P7** all-polymer OPVs afford a PCE of 1.70%, the highest to date for all-polymer solar cells employing NDI-based acceptors, either polymeric or molecular.

2. Results and Discussion

2.1. Polymer Synthesis

Polymers **P1**-**P7** were synthesized via Stille polycondensation of building block **1** with **2–5** in 26–90% yields as shown in Scheme S1, with building blocks **1–5** synthesized according to known procedures.[6b,10,22] Note that the low yield of **P6** is due to the poor solubility of this polymer in aromatic solvents. The physicochemical properties of new polymers **P1**, **P2**, **P4**-**P6**, together with **P3** and **P7** reported previously,[10] are summarized in **Table 1**. The molecular weights (M_ws) of **P1**, **P2**, **P4**, **P5**, **P6** by GPC are M_w = 78.0 KDa, (PDI = 2.3), M_w = 57.0 KDa, (PDI = 2.3), M_w = 26.0 KDa, (PDI = 1.59), M_w = 72.1 KDa, (PDI = 5.3); M_w = 9.8 K Da, (PDI = 1.5), respectively. These polymers were fully characterized by ^1H and ^{13}C NMR spectroscopy (broad features as expected), electrochemistry, optical spectroscopy, TGA, DSC, and elemental analysis (see Experimental Section for details).

2.2. Polymer Thermal Properties

Thermogravimetric analysis (TGA, heating ramp rate = 10 °C min^{-1} under N_2) was used to investigate polymer thermal properties (Figure S1, Supporting Information), with a 5% mass loss defined as the thermolysis threshold. The thermolysis onset temperature for polymer **P2** is ≈280 °C, while all other polymers have onset temperatures > 300 °C, indicative of excellent thermal stability. This characteristic allows thin film annealing and microstructure analysis to be carried out over a broad range of temperatures, 50–300 °C. The thermal properties of the new polymers were also examined by differential scanning calorimetry (DSC) and provide evidence for amorphous characteristics with no detectable endotherms or exotherms.

2.3. Optical Absorption Spectroscopy, Photoluminescence, and DFT Computation

Solution and thin-film optical absorption spectra of polymers **P1–P7** are shown in **Figure 3**, and data are collected in Table 1. Due to the presence of multiple transitions and large Stokes shifts, solution and solid state optical band gaps (E_g) were estimated from the low-energy band edges in the spectra.[23] Time-dependent DFT (TDDFT)[24] calculations at the B3LYP/6–31G** level were also performed on the polymer building blocks to provide insights into the electronic structure of the corresponding copolymers.

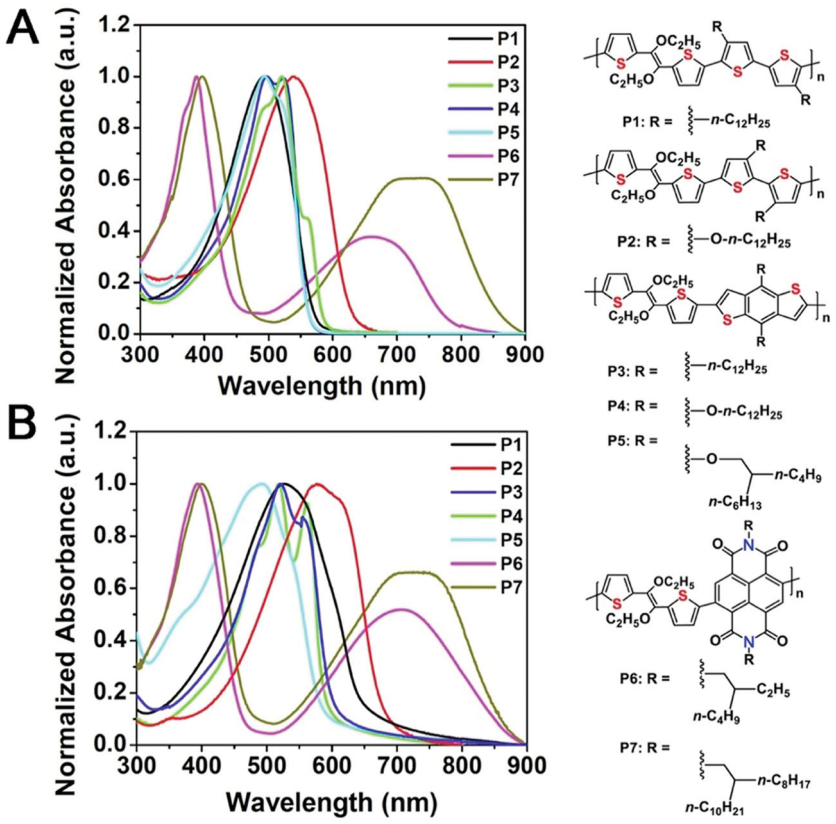

Figure 3. Optical absorption spectra of polymers **P1**-**P7**: A) in DCB solution; B) as thin films on glass substrates.

The absorption maxima of TVTOEt-T2R polymers **P1** (R = *n*-$C_{12}H_{25}$) and **P2** (R = O-*n*-$C_{12}H_{25}$) in *o*-DCB solution are located at 494 and 540 nm, respectively (Figure 3). Since both polymers have identical backbones, the absorption maximum differences must reflect electronic structure variations due to the backbone substituents and/or the different aggregation states. In fact, the DFT calculations predict a more planar skeleton and hence a more π-delocalized backbone for **P2** than for **P1**. While the **TVTOEt** comonomer exhibits the same conformation (dihedral angles ≈ 14°) in both polymers, the two rings in the bithiophene fragment are coplanar in polymer **P2** while a dihedral angle of ≈16° is predicted for **P1** between the alkoxy groups (in head-to-head linkages) and the S atoms of neighboring thiophene rings (**Figure 4**). Note that alkyl substituents in a head-to-head configuration should induce a greater distortion from planarity than observed for polymer **P1** having a tail-to-tail configuration, due to greater steric crowding (Figure 4).[25] Hence, the 46 nm bathochromic shift of **P2** vs **P1** is attributed to both the stronger *n*-$C_{12}H_{25}O$- substituent electron donor properties vs the *n*-$C_{12}H_{25}$ alkyl substituent, and the more delocalized **P2** skeleton due to the presence of four cooperative intramolecular S···O interactions which planarize the backbone, vs only two in **P1** (Figure 4). The spin-coated films of **P1** and **P2** exhibit optical absorption maxima at 528 nm and 577 nm, respectively (Figure 3). Both of these maxima exhibit large red-shifts upon going from the solution to the thin film phase, indicating a greater degree of organization in the latter. To better understand these features, TDDFT calculations were carried out on isolated comonomers with the goal of establishing energetic trends rather than comparing absolute energies. With this proviso in mind, the TDDFT calculations predict intense absorptions for both **P1** and **P2** at 448 and 489 nm, respectively. This trend is in excellent agreement with the experimental results discussed above. These strong absorptions are described theoretically as one-electron HOMO → LUMO excitations (Figure S2, Supporting Information).

The solution optical absorption maxima of TVT-BDTR polymers **P3** (R = *n*-$C_{12}H_{25}$), **P4** (R = O-*n*-$C_{12}H_{25}$), and **P5** (R = O-*i*-$C_{12}H_{25}$) are located at 520, 523, and 494 nm, respectively, while those of the corresponding thin films are located at 518 nm for **P3**, 521 nm for **P4**, and 492 nm for **P5** (Figure 3). Interestingly, the **P3** and **P4** absorption maxima are similar, with the alkoxy and alkyl chain substitution on the benzodithiophene unit having no significant effect on the energy levels of these conjugated systems. This result differs from previous reports that alkoxy substituents appended to benzodithiophenes can significantly raise the HOMO energies versus alkyl substituents.[26] Since the TDDFT calculations predict comparable wavelengths for the **P3** and **P5** absorption maxima (443 nm and 448 nm, respectively), the blue shift observed in **P5** must be attributed to supramolecular effects such as steric hindrance imposed by the bulkier branched alkyl substituents. TVTOEt-NDIR polymers **P6** and **P7** exhhibit two strong absorption bands. The shorter wavelength feature assigned to a π–π^* transition of the donor building block, while the lower energy band is assigned to a one-electron HOMO → LUMO excitation, as shown in Figure S3 (Supporting Information), implying photo-induced intra-macromolecule charge transfer (ICT) between the electron-rich TVTOEt block and the electron-deficient NDI block. The absorption maxima of **P6** and **P7** occur, respectively, at 660/388 nm and 744/396 nm in DCB solution and at 705/393 nm and 725/399 nm in spin-coated thin films. Note that the two transitions are predited theoretically at 742 (*f*: 0.2256) and 397 nm (*f*: 0.5633), in reasonable agreement with experiment. The blue shift of the **P6** absorption versus that in **P7** may reflect its lower molecular weight.

The optical band gaps for the new polymers were estimated from the low-energy band edges of the thin-film optical spectra, taking 10% of the maximum as the band edge. The optical band gaps of polymers **P1**, **P2**, **P3**, **P4**, **P5**, **P6**, and **P7** are therefore 1.83, 1.77, 2.04, 1.94, 2.07, 1.46, and 1.43 eV, respectively. This trend is similar to that predicted by the DFT calculations, which yield HOMO-LUMO gaps of 3.00, 2.74, 3.03, 3.00, 3.02, and 1.99 eV for the **P1**, **P2**, **P3**, **P4**, **P5**, and **P6** (**P7**) comonomers, respectively. Since these polymers share a common TVTOEt building block, the optical band gaps all reflect the electronic coupling with the other comonomer. For example, the band

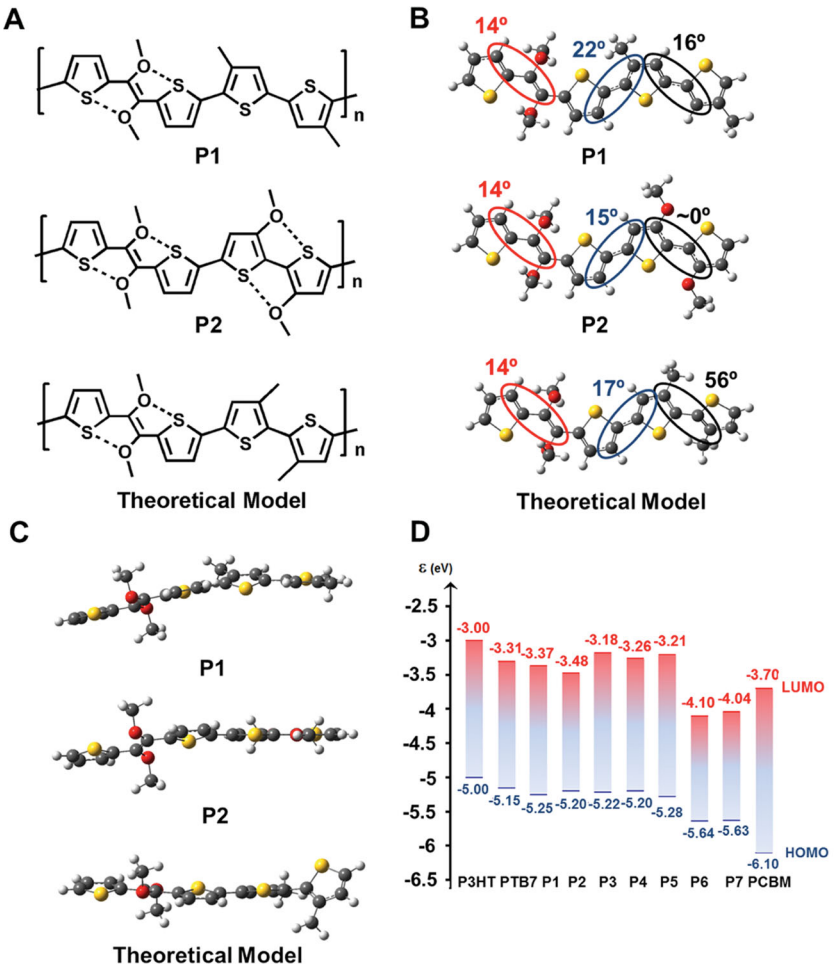

Figure 4. A) Structures of **P1**, **P2**, B) DFT//B3LYP/6–31G** computed **P1**, **P2** model polymer views perpendicular to the molecular planes; estimated dihedral angles discussed in the text are indicated by circles, and C) DFT//B3LYP/6–31G** computed **P1**, **P2** model polymer views in the molecular planes; D) Experimentally determined energy levels of **P1**–**P7**, P3HT, PTB7, and PCBM.

gap of **P2** is smaller than that of **P1**, which indicates that the bithiophene building block with alkoxy substituents is electronically richer than that with alkyl substituents, in agreement with the known electron donating effects of alkoxy substituents appended to aromatic cores.[7]

Since **P7** is intended as a polymeric acceptor for all-polymer solar cell studies (vide infra), the optical responses of **P7** blended with **P3**, P3HT, and PTB7 were investigated in detail. As shown in Figure S4 (Supporting Information), the optical absorption spectra of as-cast **P3**:**P7**, P3HT:**P7**, and PTB7:**P7** blend films are essentially superpositions of the component material spectra, suggesting that intermacromolecule charge transfer is minimal in the ground states of these polymer blends.[27] As shown in Figure S4 (Supporting Information), while pristine **P3**, P3HT, and PTB7 films exhibit strong photoluminescence (PL) in the range of 580–800, 550–800, and 700–850 nm, respectively, the blend films with **P7** show evidence of significantly quenched PL intensities, indicative of either energy or charge transfer processes. Considering that charge transfer here is thermodynamically favorable between these blend components, PL quenching is a strong indicator that this system should provide a PV response. However, the P3HT:**P7** blend films exhibit only ≈80% PL quenching, which portends relatively low PCEs for OPVs fabricated with these materials. In contrast, the nearly 100% PL quenching observed in the PTB7:**P7** blend films is encouraging for all-polymer solar cells fabricated with these materials (see more below).

2.4. Electrochemical Properties

Oxidation and reduction potentials for **P1**–**P7** were measured by cyclic voltammetry (CV) using ferrocene as the internal standard. Cyclic voltammograms of the polymers as thin films are shown in Figure S5, and electrochemical data are summarized in Table 1 and Figure 4D. From these potentials and the optical bandgaps, HOMO and LUMO energies can be estimated.[5c] For example, the HOMO energy levels of TVT-T2R derivatives **P1** and **P2** lie at –5.25 and –5.20 eV, respectively, with the slightly higher HOMO energy of **P2** attributable to the stronger electron donating character of the thiophene alkoxy substituents (-O-*n*-$C_{12}H_{25}$). Using the optical band gaps, the corresponding LUMO energies for **P1** and **P2** are estimated at –3.37 and –3.48 eV, respectively. The HOMO energies of the TVTOEt-BDTR polymers **P3**, **P4**, and **P5** lie at –5.22, –5.20, and –5.28 eV, respectively, and the corresponding LUMO energies lie at –3.18, –3.26, and –3.21 eV, respectively, using the aforementioned optical band gap estimation. The similar HOMO energies of **P3** and **P4** show that the alkoxy and alkyl functionalization of the BDT building block minimally influences the electronic structure. However, the HOMO energy difference between **P3** and **P4** versus **P5** is attributed to the steric demands of the bulky substituents. The less bulky linear substituents on **P3** and **P4** promote closer intermolecular packing and destabilize the HOMO levels. In contrast, the HOMO energies of TVTOEt-NDIR-based polymers **P6** and **P7** lie at –5.64 and –5.63 eV, respectively, with the corresponding LUMOs at –4.10 and –4.04 eV, respectively. Interestingly, the rather low-lying **P7** LUMO is similar in energy to that of $PC_{70}BM$ (–4.3 eV),[28] indicating that **P7** could serve as both a good n-channel semiconductor as well as an effective electron acceptor in OPV devices.

2.5. Thin-Film Transistor Characterization

Top-contact/bottom-gate OTFTs of structure HMDS-SiO_2/p^+-Si/polymer/Au contacts were evaluated both in ambient and vacuum to assess the majority charge carrier type, device performance, and environmental stability. The field-effect

Table 2. Field-effect mobilities (μ), threshold Voltages (V_T), and current I_{on}/I_{off} ratios for thin films transistors of polymers **P1**-**P7**. Device parameters are average values of at least 16 devices.

Polymer	Structure	μ [cm^2 V^{-1} s^{-1}]	I_{on}/I_{off}	V_T [V]	λ_{reorg} [eV]
P1	**P4:** R = –O-*n*-$C_{12}H_{25}$	3×10^{-3}	6×10^3	–25	0.39
P2	**P5:** R = –O–(*n*-C_4H_9, *n*-C_6H_{13})	8×10^{-4}	10^4	–15	0.37
P3[a]	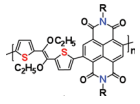	0.02	5×10^5	–15	0.31
P4		3×10^{-4}	10^4	–5	0.47
P5		5×10^{-5}	10^4	–15	0.49
P6	**P6:** R = –C_2H_5, *n*-C_4H_9; **P7:** R = *n*-C_8H_{17}, *n*-$C_{10}H_{21}$	7×10^{-3}	10^2	25	0.31
P7[a]		0.1–0.2	10^6	15	0.31

[a]The device data are from Ref. [10].

mobility and threshold voltages were calculated in the saturation regime. TFT data are summarized in **Table 2**, and representative transfer plots are shown in **Figure 5** and Supporting Information Figures S6–S8. Furthermore, to understand charge transport efficiencies, the morphology and microstructure of the thin films used in the TFTs were also investigated by AFM and XRD. Additionally, a crucial electronic structure parameter is the intramolecular reorganization energy, which describes the energy required to accommodate a charge unit in the transport process and typically correlates with charge mobility. This parameter involves two terms associated with the geometric relaxation energies upon going from neutral to charged species and vice versa, and is computed from the corresponding adiabatic potential energy surfaces.[29] Thus, reorganization energies for the present polymers were calculated for holes λ_h and electrons λ_e, depending on the TFT response, to better understand the charge transport process as shown in Table 2. The λ_h of **P1**(0.39 eV) is slightly larger than that of **P2** (0.37 eV). This indicates that the differences in their mobilities are likely determined by other film parameters. However, the λ_h of **P3** (0.31 eV) is much smaller than those of **P4** (0.47 eV) and **P5** (0.49 eV), which suggests that the mobility of **P3** may be higher than those of **P4** and **P5**. Interestingly, these reorganization energies correlate well with the charge transport results, which are discussed below.

As shown in Table 2, Figure S6 and S7, the hole mobilities of TVTOEt-T2R polymers **P1** and **P2**, after annealing at 90 °C are 3.2×10^{-3} and 7.5×10^{-4} cm^2 V^{-1} s^{-1}, respectively. These modest values are not surprising since the XRD analysis indicates that both film types are amorphous. Note that **P2** has a lower mobility than **P1** despite having a more planar backbone, higher HOMO energy, and lower λ_h (0.39 and 0.37 eV for **P1** and **P2**, respectively), suggesting that morphological factors may dominate the transport characteristics. Regarding the TVTOEt-BDTR polymers, the hole mobilities of **P3**, **P4**, and **P5** are 2.0×10^{-2}, 3.0×10^{-4}, and 2.5×10^{-4} cm^2 V^{-1} s^{-1}, respectively (Figures 5 and Figure S6, Supporting Information). Since **P3**, **P4**, and **P5** have indentical backbones, the differences in mobilities can be attributed to peripheral substituent effects,[30] and the DFT computed reorganization energies are in full agreement with the TFT performance (Table 2). Thus, **P3** with the lowest λ_h within this family (0.31 eV), is in agreement with having the largest hole mobility, 2.0×10^{-2} cm^2 V^{-1} s^{-1}. In contrast, the lowest mobility of **P5** (2.5×10^{-4} cm^2 V^{-1} s^{-1}) also has the highest reorganization energy (0.49 eV). Therefore, it is evident that the alkyl (linear) and alkoxy (branched) peripheral substituents can influence the reorganization energies and the charge transport properties of these conjugated polymers.

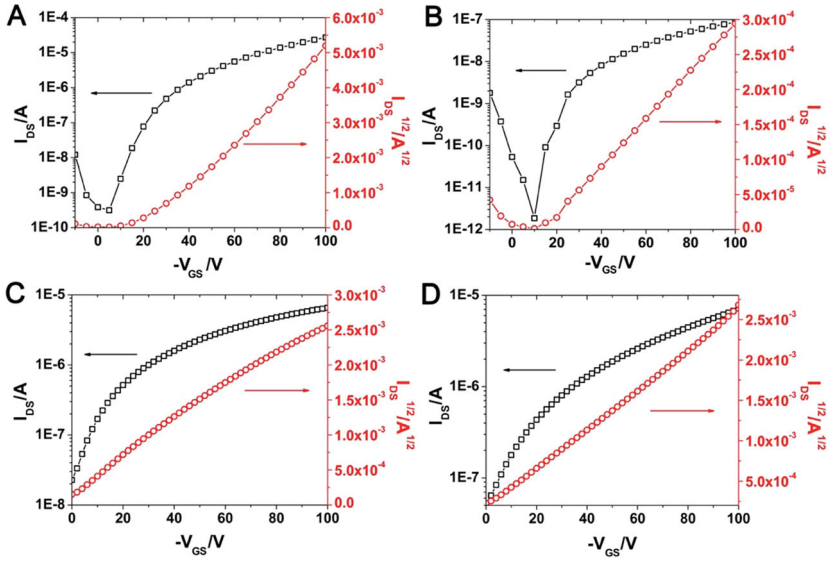

Figure 5. OTFT transfer plots of A) polymers **P3** and B) **P5** at V_{SD} = –100 V; and PTB7:**P7** polymer as-cast blend TFTs in: **C**) p-type operation mode and **D**) n-type operation mode.

To better understand the OTFT transport trends, XRD and AFM analyses were also carried out for films of **P3** and **P5**. As shown in **Figure 6**, the **P3** film exhibits a single diffraction peak without obvious reflections associated with in-plane π–π stacking.

The corresponding d-spacings of 19.0 and 13.4 Å reflect the different alkyl substituents steric demands. The higher reflection intensity of **P3** vs **P5** indicates a higher degree of order, consistent with the mobility trends. The AFM topographic images of the **P3**

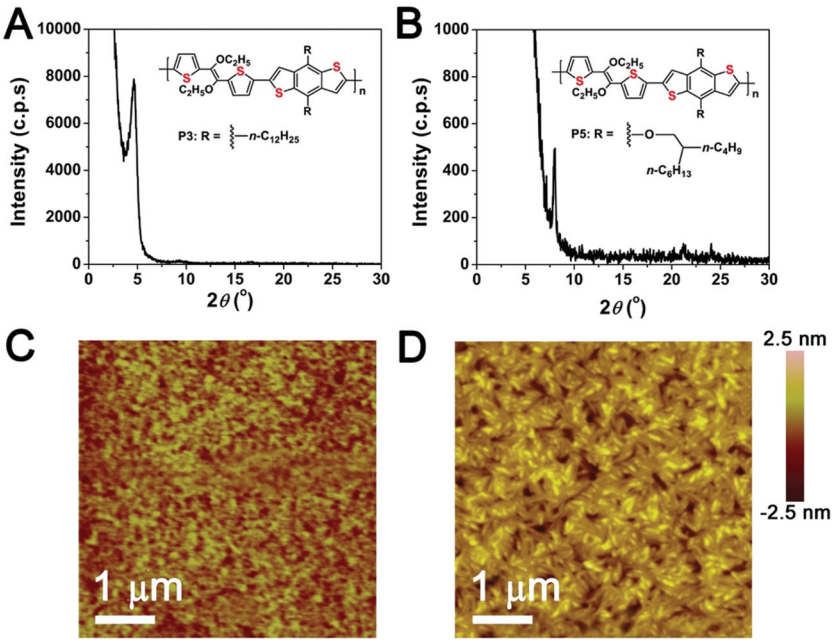

Figure 6. θ-2θ X-ray diffraction (XRD) scans of A) spin-coated **P3** and B) **P5** thin films after annealing at 150 °C. Peak intensities are not normalized. Tapping mode AFM images of C) **P3** and D) **P5** thin films after annealing at 150 °C (scan areas: 4.5 μm × 4.5 μm).

films corroborates the XRD data (Figure 6C) indicating distinct domain formation. However, the **P5** film morphology is less ordered (Figure 6D) and characterized by significant defects (dark holes) and irregularities which might depress charge transport. The enhanced crystallinity, improved morphology, and reduced λ_h are thus in accord with the higher mobility (≈1000×) of **P3** versus that of **P5**.

Combining the NDIR building block with the TVTOEt monomer affords air stable n-type polymers. The electron mobilities of **P6** and **P7** are 7.0×10^{-3} and 0.2 $cm^2\ V^{-1}\ s^{-1}$, respectively (Figure S6, Supporting Information).[10] These transport differences are consistent with the XRD data on the corresponding films (Figure S10, Supporting Information), which show that the **P7** films exhibit much sharper and stronger reflections with a *d*-spacing of ≈22.2 Å. This distance is reasonably assigned to *a*-axis (*h*00) lamellar spacing, indicating a more ordered microstructure. In comparison, the **P6** films show a broader peak with a lamellar *d*-spacing of ≈14.7 Å. Both distances are consistent with structural models in which the polymer side chains are either interdigitated or closely packed, and tilted from the molecular plane, implicating a polymorph in which most molecules have an edge-on orientation with respect to the substrate, and with the π–π stacking axis parallel to the substrate plane, thus favoring in-plane source → drain charge transport.[31] The difference in *d*-spacing is attributed to the different alkyl peripheral subsituents on the NDI block, where the longer **P7** branched alkyl chains induce larger *d*-spacings. Furthermore, the much smaller molecular weight and reduced **P6** solubility may also contribute to the poorer film quality and therefore lower electron mobility. DFT calculations also predict a low λ_e of 0.31 eV for these TVTOEt-NDIR polymers, which is comparable to those reported for other efficient n-type semiconductors.[29a,32]

Finally, since **P3**:**P7**, P3HT:**P7**, and PTB7:**P7** blends will be used for BHJ OPV devices (vide infra), TFTs based on the same blend composition yielding optimal OPV performance (weight ratio = 1:1, $CHCl_3$) were fabricated and characterized. TFTs were also fabricated using various processing conditions in accord with OPV device optimization, (Table S1, Supporting Information) and the data are summarized in Table S2. The ambipolar nature of these TFTs, in both electron and hole modes, is evident from the *I*–*V* characteristics. The TFTs based on **P3**:**P7** blend as-cast films exhibit electron and hole mobilities of 1.4×10^{-4} $cm^2/V \cdot s$ and 2.4×10^{-4} $cm^2\ V^{-1}\ s^{-1}$, respectively (Figure S8, Supporting Information). After annealing at 120 °C for 10 min, the TFTs exhibit higher and more balanced ambipolarities ($\mu_e = 4.5 \times 10^{-4}$ $cm^2\ V^{-1}\ s^{-1}$ and $\mu_h = 6.4 \times 10^{-4}$ $cm^2\ V^{-1}\ s^{-1}$), indicating that this material is a better candidate for all-polymer OPVs after annealing. This annealing effect on TFT performance is also observed for the P3HT:**P7** blend. Here TFTs based on the as-cast films evidence unbalanced electron and hole mobilities with $\mu_e = 2.5 \times 10^{-4}$ $cm^2\ V^{-1}\ s^{-1}$ and $\mu_h = 9.0 \times 10^{-5}$ $cm^2\ V^{-1}\ s^{-1}$. However, after annealing at 120 °C for 10 min, the TFTs exhibit larger, more balanced electron and hole mobilities (Figure S9). The derived saturation mobilities are $\mu_e = 1.0 \times 10^{-4}$ $cm^2\ V^{-1}\ s^{-1}$ and $\mu_h = 2.0 \times 10^{-4}$ $cm^2\ V^{-1}\ s^{-1}$. However, further annealing at 150 °C/10 min does not improve the performance ($\mu_e = 4.2 \times 10^{-5}$ $cm^2\ V^{-1}\ s^{-1}$ and $\mu_h = 1.6 \times 10^{-4}$ $cm^2\ V^{-1}\ s^{-1}$). In contrast, annealing has different effects on the properties of the PTB7:**P7** blends. Here TFTs based on the as-cast films exhibit high, well-balanced electron and hole mobilities of $\mu_e = 5.1 \times 10^{-3}$ $cm^2\ V^{-1}\ s^{-1}$ and $\mu_h = 3.9 \times 10^{-3}$ $cm^2\ V^{-1}\ s^{-1}$ (Figure 5). To the best of our knowledge, these mobilities are among the highest reported for all-polymer bulk heterojunction TFTs.[33] However, after annealing at 120 °C for 10 min, the TFT mobilities fall to $\mu_e = 1.4 \times 10^{-3}$ $cm^2\ V^{-1}\ s^{-1}$ and $\mu_h = 1.1 \times 10^{-3}$ $cm^2\ V^{-1}\ s^{-1}$ (Figure S9, Supporting Information). It will be shown that these transport results are consistent with the corresponding OPV performance (vide infra).

2.6. All-Polymer Photovoltaic Cell Characterization

To evaluate **P7** performance as a polymeric OPV electron acceptor, P3HT:**P7**, **P3**:**P7**, and PTB7:**P7** bulk heterojunction cells based on these blends were fabricated in both a conventional device structure, ITO/PEDOT:PSS/blend/LiF/Al, and in an inverted device structure, ITO/ZnO/blend/MoO_3/Ag. Measurements were carried out under simulated AM 1.5 G illumination of 100 mW cm^{-2}. *J*–*V* curves and external quantum efficiency (EQE) data are shown in **Figures 7** and Supporting Information (Figure S10). The corresponding open-circuit voltages (V_{oc}), short-circuit currents (J_{sc}), fill factors (FF), and

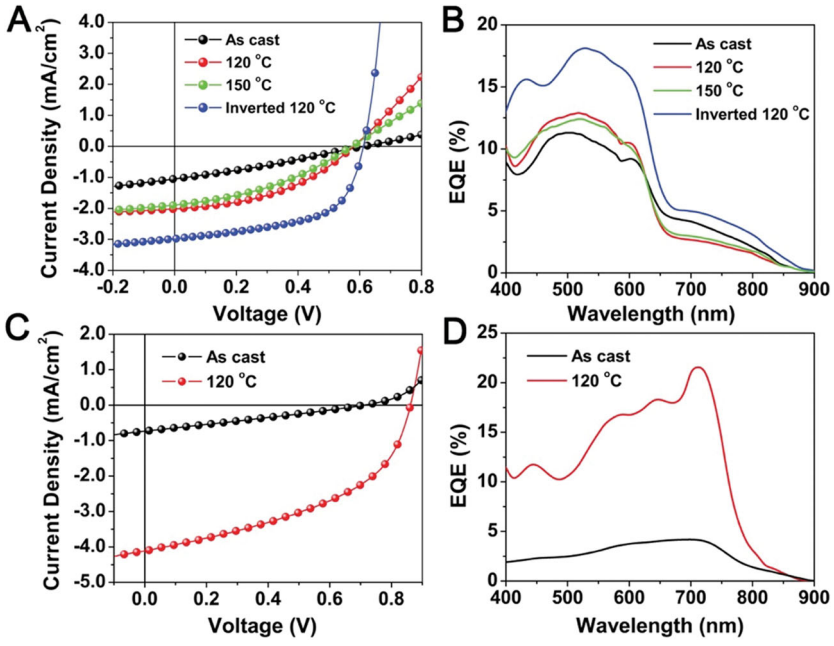

Figure 7. *J–V* characteristics of A) P3HT:**P7** and C) PTB7:**P7**-based solar cells under AM 1.5 solar illumination and external quantum efficiencies of the B) P3HT:**P7** and D) PTB7:**P7**-based solar cells (120 °C: anneal at 120 °C; 150 °C: anneal at 150 °C; Inverted-120 C: anneal at 120 °C with an inverted device structure).

power conversion efficiencies (PCE) are summarized in **Table 3** and Supporting Information Figure S1.

Starting with the as-cast P3HT:**P7** films, the all-polymer OPVs yield the following metrics for a conventional structure: PCE = 0.18%, V_{oc} = 0.61 V, J_{sc} = 1.05 mA cm^{-2}, fill factor (FF) = 0.29. Annealing the P3HT:**P7** blend films at various temperatures was employed to optimize the performance, with 120 °C affording: PCE = 0.50%, V_{oc} = 0.58 V, J_{sc} = 2.02 mA cm^{-2}, FF = 0.42. Note that the optimized devices yield PCEs ≈2× that of P3HT/PNDI2OD-T2 blends using the same processing solvent.[34] The increased J_{sc} upon annealing can be attributed to greater structural order (vide infra), and the increased FF is consistent with the balanced hole and electron mobilities observed in the annealed blend, as the TFT measurements indicate. However, after annealing the P3HT:**P7** films at 150 °C before electrode deposition, V_{oc} falls slightly to 0.58 V, J_{sc} to 1.89 mA cm^{-2}, FF to 0.37, and PCE to 0.41%. The decrease in PCE can be attributed to rougher films (vide infra) and unbalanced hole and electron mobilities, as observed in the TFT devices. The EQE response generally tracks the optical spectrum of the blend rather than that of the P3HT film alone, with light harvesting beyond 650 nm attributable to **P7** (Figure 7B). To enhance performance, an inverted ITO/ZnO/P3HT:**P7**/MoO_3/Ag OPV structure[17d,e] was employed. After annealing at 120 °C, the PCE dramatically increases to 1.06% with V_{oc} = 0.61 V, J_{sc} = 2.99 mA cm^{-2}, FF = 0.58 (Figure 7).

Similar efficiency enhancement upon annealing is also observed for the **P3**:**P7** blend-based OPVs. For the as-cast films, devices with inverted structures afford a low PCE of only 0.08% with a V_{oc} = 0.75 V, J_{sc} = 0.39 mA cm^{-2}, FF = 0.26 (Figure S11, Supporting Information). However, after annealing at 120 °C for 10 min, the efficiency dramatically increases to 0.49% with V_{oc} = 0.85 V, J_{sc} = 1.51 mA cm^{-2}, *FF* = 0.39. Despite this modest overall performance, this is the first time that the same building block (TVTOEt) has been used as the contituent block for both donor and acceptor components of a polymer-polymer blend OPV. Again, the performance can be correlated with the improved microstructural order (vide infra) and TFT transport characteristics.

Finally, for PTB7:**P7** cells, the efficiency of an inverted architecture device with as-cast films is 1.70% with V_{oc} = 0.86 V, J_{sc} = 4.11 mA cm^{-2}, FF = 0.46, which is the highest PCE reported to date for NDI-based OPVs (either polymer or small molecule; Figure 7), although others report similar but lower efficiency.[19f,g,35] The high V_{oc} is remarkable since the $HOMO_{PTB7}$-$LUMO_{P7}$ offset is only 1.11 eV. Note however that this is a preliminary result and the poor fill factor suggests that the PCE should be improvable with further device optimization. Not surprisingly, annealing is detrimental to PTB7:**P7** OPV performance, consistent with the TFT results. After annealing at 120 °C for 10 min, the PCE falls dramatically to 0.13% with a V_{oc} = 0.76 V, J_{sc} = 0.61 mA cm^{-2}, and FF = 0.27. This significant decrease is attributed to the obvious morphology changes upon annealing (vide infra).

AFM and XRD analyses were employed to characterize the thermal annealing effects on the blend microstructures and to help understand the trends in OPV performance. In general, polymer mixtures tend to undergo phase segregation due to low entropies of mixing,[36] and phase segregation is clearly evident even before annealing, as indicated by well separated dark and bright domains (**Figure 8**). The large film domains (>200 nm) exceed typical exciton diffusion lengths and are expected to result in low current densities. For the P3HT:**P7** blends, after thermal annealing at 120 °C or 150 °C, the blend film morphologies show no obvious morphological changes as characterized by AFM. The XRD data indicate that the blend film is amorphous before annealing (Figure 8D) and after annealing at 120 °C, a broad Bragg reflection appears (Figure 8E), indicating greater ordering in accord with the balanced TFT mobilities and optimal PV performance. The calculated *d*-spacing is ≈30.5 Å, which is assignable to the (100) reflection of P3HT or **P7** in the blend film—much larger than that of the pristine film

Table 3. OPV device characteristics of P3HT:**P7**, P3:**P7**, and PTB7:**P7** blend-based All-polymer solar cells.[a)]

Blend	J_{sc} [mA cm^{-2}]	V_{oc} [V]	FF	PCE [%]
P3HT:**P7**[b)]	2.99	0.61	0.58	1.06
P3:**P7**[b)]	1.51	0.85	0.39	0.49
PTB7:**P7**[c)]	4.11	0.86	0.46	1.70

[a)]The solar cells have an inverted struture of ITO/ZnO/blends/MoO_3/Ag; [b)]The film was annealled at 120 °C for 10 min; [c)]As-cast film.

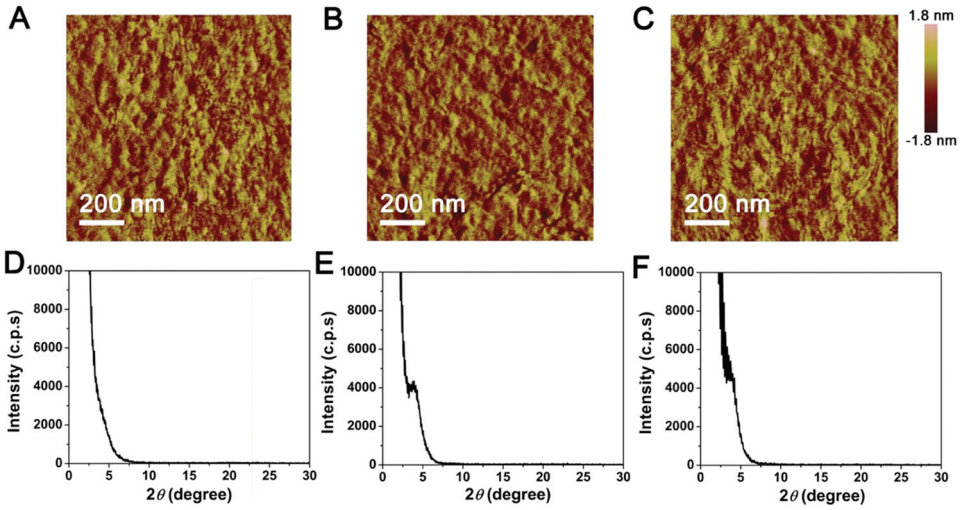

Figure 8. Tapping mode AFM images (1 μm × 1 μm) and θ–2θ XRD scans of P3HT:**P7** thin films A,D) before and B,E) after annealing at 120 °C and C,F) 150 °C for 10 min.

component (P3HT: 15.1 Å;[37] **P7**: 22.2 Å). However, this reflection broadens upon further annealing at 150 °C (Figure 8F), indicating decreased ordering, in agreement with the decreased PCE of the corresponding OPV devices.

Similar annealing effects are observed for the **P3**:**P7** blends. Although there are no obvious microstructural changes in the AFM images, the film XRD reflection intensity of (100) peak increases dramatically from 5000 to 40 000 counts upon annealing at 120 °C for 10 min (Figure S12, Supporting Information). This indicates far more ordered films in accordance with the greater PCEs of the annealled **P3**:**P7** based solar cells. Also, the *d*-spacing distance slightly increases from 20.7 Å to 21.5 Å after annealing. Both distances are close to that of the pristine **P7** films (22.2 Å), indicating that the top surface is **P7**-rich, which is consistent with the XPS depth profiling data (Figure S13, Supporting Information). XPS depth profiling measurements were used to probe the relative N1s content on proceeding from the air/BHJ interface, through the active layer, to the buried active layer/ZnO interface.[38] Changes in N1s content indicate vertical phase segregation, where the blend film has a P7-rich top interface. This phenomenon has been observed in other bulk heterojunction all-polymer blend OPV systems.[35a] For the PTB7:**P7** blends, obvious morphology changes are observed in the AFM after annealling (Figure S14, Supporting Information) although the films under both conditions are amorphous according to XRD measurements. The darker regions in the AFM images become significantly larger, which presumably indicates film microstructural reorganization. The resulting large domain sizes could impede exciton dissociation and charge collection properties. Thus, it is not surprising that the efficiency here falls dramatically upon annealling.

3. Conclusions

A new series of p- and n-type semiconducting polymers incorporating the TVTOEt moiety has been synthesized and characterized. The effects of co-monomer incorporation (T2, BDT, and NDI) with TVTOEt and peripheral substitution (alkyl vs alkoxyl; linear chain vs branched chain) on the thin film microstructure and OTFT/OPV device performance were also investigated. It is found that incorporation of functional groups into the polymer backbone significantly influences both the electronic energy levels and thin film morphologies of these polymers. For example, using the same conjugated backbone results in a hole mobility 100 × greater for **P3**, which contains linear side-chains, than that of **P5**, which is substituted with alkoxyl branched side chains. Ambipolar bulk heterojunction OTFTs and all-polymer OPVs were also fabricated with **P3**:**P7**, P3HT:**P7**, and PTB7:**P7** blends. Strong PL quenching was observed for most of the blends, implying efficient photoinduced charge separation. Thermal annealing of the blend films plays a key role in optimizing solar cell performance. Most significantly, the blend PTB7:**P7** affords not only the highest charge carrier mobilities among these ambipolar bulk heterojunction OTFTs, but also the highest PCEs reported to date for all-polymer OPVs based on an NDI-based electron acceptor. These results show that these n-type polymers are promising for all-polymer solar cells and instructive for understanding new synthetic strategies and the electrical properties of all-polymer OPV blends.

4. Experimental Section

General: All reagents were purchased from commercial sources and used without further purification unless otherwise noted. Anhydrous THF was distilled from Na/benzophenone. Conventional Schlenk techniques were used, and reactions were carried out under N_2 unless otherwise noted. Optical spectra were recorded on a Cary Model 1 UV-Vis spectrophotometer. Fluorescence measurements were recorded on a Photon Technology International model QM-2 fluorimeter. NMR spectra were recorded on a Varian Unity Plus 500 spectrometer (^{1}H, 500 MHz; ^{13}C, 125 MHz). GPC analyses of polymer samples were performed on a Waters Alliance GPCV 2000 (3 columns, Waters Styragel HT 6E, HT 4, HT 2; operation temperature, 150 °C; mobile phase, 1,2,4-trichlorobenzene or THF at room temperature; flow rate, 1 mL min^{-1}) and are reported relative to Aldrich polystyrene standards. Electrospray mass spectrometry was performed with a Thermo Finnegan model LCQ Advantage

mass spectrometer. Electrochemistry was performed on a C3 Cell Stand electrochemical station equipped with BAS Epsilon software (Bioanalytical Systems, Inc., Lafayette, IN). XRD measurements were performed on an 18 kW Rigaku ATXG diffractometer using a multilayer parabolic mirror, a $NaIS_3$ scintillation detector, and X-rays of wavelength $\lambda = 1.541$ Å. AFM measurements were performed on a Dimension Icon Scanning Probe Microscope (Veeco) in tapping mode. XPS (Omicron ESCA Probe) depth profiling is performed on actual devices prepared without the top electrode: ITO/ZnO/P3:P7 blend film. The samples are sputtered with an Ar+ gun at 3000 eV for 100 s intervals and etched from air/blend interface. Signals from C1s and N1s were monitored and integrated peak areas were used for data analysis.

Synthesis of ***P1***: Under Ar, a mixture of 2,2′-dibromo-3,3′-bisdodecyl-5,5′-bithiophene (68.1 mg, 0.10 mmol), 5,5′-bis(trimethylstannyl)-(1,2-bis(2′-thienyl)-1,2-diethoxyvinyl (62.5 mg, 0.10 mmol), tri(*o*-tolyl)phosphine (5.0 mg, 0.016 mmol), and tris(dibenzylideneacetone)-dipalladium(0) (3.8 mg, 0.004 mmol) in anhydrous toluene (15 mL) was stirred at reflux for 48 h. Bromobenzne (0.3 mL) was then added, and this mixture was refluxed for additional 10 h. After cooling to room temperature, the reaction mixture was poured into a mixture of methanol (100 mL) and concentrated HCl solution (5 mL), and the precipitate was collected by filtration. This isolated crude product was then subject to Soxhlet extraction with methanol, acetone, and hexane in sequence. Finally, the product was extracted with chloroform, and the extract was concentrated before it was precipitated with methanol again, leading to a dark red solid as the product (63.0 mg, 78.5%). ^{1}H NMR ($CDCl_3$, 500 MHz): δ: 7.28 (s, br, 2H), 7.13 (s, br, 2H), 7.04 (s, br, 2H), 3.97 (m, br, 4H), 2.82 (m, br, 4H), 1.73 (m, br, 4H), 1.51 (m, br, 6H), 1.44 (m, br, 4H), 1.22–1.38 (m, br, 32H), 0.85–0.91 (t, J = 7.0 Hz, 6H). GPC: M_n = 34.3 K Da, M_w = 78.0 K Da, PDI = 2.3. Elemental Analysis: calc. C, 70.90; H, 8.54; N, 0.00; found C, 70.55; H, 8.39; N, 0.00.

Synthesis of ***P2***: Under N2, a mixture of BTOC12-Br2 (60.2 mg, 0.087 mmol), 5,5′-bis(trimethylstannyl)-(1,2-bis(2'-thienyl)-1,2-diethoxyvinyl (52.8 mg, 0.087 mmol), and $Pd(PPh_3)_2Cl_2$ (3.0 mg, 0.004 mmol) in anhydrous toluene (10 mL) was stirred at 100 °C for 48 h. Bromothiophene (1.0 mL) was then added and the resulting mixture was stirred for an additional 10 h. After cooling to room temperature, the reaction mixture was poured into methanol (150 mL), and the resulting mixture was stirred for 30 min, before it was filtered. The obtained solid product was washed with methanol and acetone, and then subjected to Soxhlet extraction with methanol, acetone, and hexane in sequence. Finally the product was extracted with chloroform, and the extract was concentrated. The residue was taken up with chloroform, and this solution was precipitated with methanol twice, leading to a purple solid as the product (30 mg, 77%). ^{1}H NMR ($CDCl_3$, 500 MHz): δ: 7.24 (s, br, 2H), 7.15 (s, br, 2H), 6.98 (s, br, 2H), 4.21 (s, br, 4H), 3.96 (s, br, 4H), 1.95 (m, br, 4H), 1.58 (s, br, 8H), 1.51–1.21 (m, br, 34H), 0.89 (m, br, 6H). ^{13}C NMR ($CDCl_3$, 125.7 MHz, 25 °C): δ 152.2; 140.5; 138.9; 134.5; 132.8; 126.3; 122.3; 113.9; 112.2. GPC: M_n = 24.6 K Da, M_w = 57.0 K Da, PDI = 2.3. Elemental Analysis: calc. C, 68.10; H, 8.20; found, C, 66.77; H, 7.85.

Synthesis of ***P4***: Under N_2, a mixture of BDTOC12-Br2 (107 mg, 1.49 mmol), 5,5′-bis(trimethylstannyl)-(1,2-bis(2'-thienyl)-1,2-diethoxyvinyl (91 mg, 1.49 mmol), and $Pd(PPh_3)_2Cl_2$ (6.0 mg, 0.008 mmol) in anhydrous toluene (10 mL) was stirred at 100 °C for 48 h. Bromothiophene (1 mL) was then added and the resulting mixture was stirred for an additional 10 h. After cooling to room temperature, the reaction mixture was poured into methanol (150 mL), and the resulting mixture was stirred for 30 min, before it was filtered. The obtained solid product was washed with methanol and acetone, and then subjected to Soxhlet extraction with methanol, acetone, and hexane in sequence. Finally the product was extracted with chloroform, and the extract was concentrated. The residue as taken up with chloroform, and this solution was precipitated in methanol twice, leading to a red solid as the product (100 mg, 80%). ^{1}H NMR ($CDCl_3$, 500 MHz): δ: 7.66 (s, br, 2H), 7.32 (s, br, 4H), 4.33 (s, br, 4H), 3.00 (s, br, 4H), 1.95 (m, br, 4H), 1.62–1.21 (m, br, 44H), 0.89 (m, br, 6H). ^{13}C NMR ($CDCl_3$, 125.7 MHz, 25 °C): δ 143.9; 140.9; 138.3; 136.7; 136.1; 132.7; 129.5; 126.6; 12.1; 115.9. GPC: M_n = 16.4 K Da, M_w = 26.0 K Da, PDI = 1.59. Elemental Analysis : calc. C, 69.01; H, 7.96; found C, 70.44; H, 7.67.

Synthesis of ***P5***: Under Ar, a mixture of 2,6-diiodo-4,8-bis(2-butyloctyloxy)benzo[1,2-b;3,4-b]dithiophene (109.3 mg, 0.14 mmol), 5,5′-bis(trimethylstannyl)-(1,2-bis(2′-thienyl)-1,2-diethoxyvinyl (81.7 mg, 0.14 mmol), tri(*o*-tolyl)phosphine (4.9 mg, 0.016 mmol), and tris(dibenzylideneacetone)dipalladium(0) (3.7 mg, 0.004 mmol) in anhydrous toluene (15 mL) was stirred at refluxing for 48 h. Bromobenzene (0.4 mL) was then added, and this mixture was refluxed for additional 12 h. After cooling to room temperature, the reaction mixture was poured into a mixture of methanol (100 mL) and concentrated HCl solution (5 mL), and the precipitate was collected by filtration. The isolated crude product was then subjected to Soxhlet extraction with methanol, acetone, and hexane. Finally, the product was extracted with chloroform, and the extract was concentrated before it was precipitated with methanol again, affording a dark red solid as the product (71.0 mg, 63.1%). GPC: M_n = 13.5 K Da, M_w = 72.1 K Da, PDI = 5.3. Elemental Analysis: calc. C, 69.02; H, 7.96; N, 0.00; found C, 68.84; H, 7.88; N, 0.00. 1H NMR ($CDCl_3$, 500 MHz): 7.55 (s, br, 2H), 7.32 (s, br, 4H), 4.21 (s, br, 4H), 3.99 (s, br, 4H), 1.92 (s, br, 2H), 1. 69 (s, br, 4H), 1.20–1.60 (m, br, 34H), 1.00 (m, br, 6H), 0.92 (m, br, 6H).

Synthesis of ***P6***: Under Ar, a mixture of NDI2EH-Br2 (68.6 mg, 0.11 mmol), 5,5′-bis(trimethylstannyl)-(1,2-bis(2′-thienyl)-1,2-diethxoyvinyl (64.1 mg, 0.11 mmol), and $Pd(PPh_3)_2Cl_2$ (3.0 mg, 0.004 mmol) in anhydrous toluene (15 mL) was stirred at 90 °C for 40 h. Bromobenzene (1 mL) was then added and the resulting mixture was stirred for an additional 4 h. After cooling to room temperature, the reaction mixture was poured into methanol (150 mL), and the resulting mixture was stirred for 30 min, before it was filtered. The obtained solid product was washed with methanol and acetone, and then subjected to Soxhlet extraction with methanol, acetone, and hexane in sequence. Finally the product was extracted with chloroform, and the extract was concentrated. The residue was taken up with chloroform, and this solution was precipitated with methanol twice, leading to a blue solid as the product (21. 4 mg, 26.3%). ^{1}H NMR ($CDCl_3$, 500 MHz): δ: 8.85 (s, br, 2H), 7.44 (s, br, 2H), 7.38 (s, br, 2H), 4.09 (m, br, 8H), 1.95 (m, br, 2H), 1.52 (m, br, 6H), 1.20–1.45 (m, br, 16H), 0.80–0.96 (m, br, 12H). GPC: M_n = 6.6 K Da, M_w = 9.8 K Da, PDI = 1.5. Elemental Analysis: calc. C, 68.90; H, 6.57; N, 3.65; found C, 67.45; H, 6.46; N, 3.56.

OTFT Fabrication: Thin semiconductor films were deposited by spin-coating of a 10 mg mL^{-1} polymer solution in chloroform under ambient conditions onto hexamethyldisilazane (HMDS)-treated p-doped Si (001) wafers with a 300 nm thermally grown SiO_2 dielectric layer. The capacitance of the 300 nm SiO_2 gate insulator was 10 nFcm^{-2}. Prior to substrate treatment with HMDS, the wafers were solvent cleaned by sonicating (in two beakers, sequentially, for 15 min each) in EtOH and were then dried with a filtered stream of N_2, followed by 5 min. plasma cleaning in a Harrick PDC-32G Plasma Cleaner/Sterilizer. After semiconductor deposition, the films were annealed at different temperatures under vacuum for 30 min. Top-contact OTFTs were fabricated by vapor deposition of gold electrodes (~10^{-7} Torr, 0.2 Å/s, ≈50 nm thick) onto the semiconductor thin films through a shadow mask to obtain devices with channel widths and lengths of 5000 μm and 100 μm, respectively.

OTFT Characterization: *I–V* plots of device performance were measured in ambient or under vacuum; at least five transfer and output plots were recorded for each device. The current–voltage (*I–V*) characteristics of the devices were measured using a Keithley 6430 subfemtoammeter and a Keithly 2400 source meter, operated by a local Labview program and GPIB communication. Key device parameters, such as charge carrier mobility (μ) and on-to-off current ratio (I_{on}/I_{off}) were extracted from the source–drain current (I_{SD}) versus source–gate voltage (V_{SG}) characteristics employing standard procedures. Mobilities were obtained from the formula defined by the saturation regime in transfer plots, $\mu = 2\ I_{SD}L/[C_iW\ (V_{SG} - V_T)^2]$, where V_T is the threshold voltage. Threshold voltage was obtained from the x intercept of V_{SG} versus $I_{SD}^{1/2}$ plots.

*Conventional Structures for ITO/PEDOT:PSS/P3HT(**P3** or PTB7):**P7** (1:1 w/w; 80 nm)/LiF/Al*: The precoated ITO glass substrates were cleaned with acetone and isopropyl alcohol under sonication, followed by drying and UV/ozone treatment over 10 min. A 30 nm layer of PEDOT:PSS was then spun-cast onto the ITO substrate and baked at 150 °C for 20 min. An ≈80–100 nm thick active layer was next prepared using various conditions mentioned above and spun-cast onto the PEDOT:PSS layer, and then thermal annealing was performed by placing the spin-coated films on a hot plate at 120 or 150 °C for 10 min. The LiF (10 nm)/Al(100 nm) cathode was finally deposited by thermal evaporation under high vacuum (10^{-6} mbar) through a shadow mask. The cell size, defined by the spatial overlap of the ITO anode and LiF/Al cathode was 6 mm^2.

*Inverted Structures for ITO/ZnO/P3HT(**P3** or PTB7)*: ***P7** (1:1 w/w; 80 nm)/MoO_x/Ag*: The precoated ITO glass substrates were cleaned as above. Afterwards, the ZnO electron transport/hole blocking layer was prepared by spin-coating at 5000 rpm from a ZnO precursor solution prepared from 0.5 M zinc acetate dehydrate in 0.5 M monoethanolamine and 2-methoxyethanol. After cleaning the electrical contacts, the substrates were immediately baked in air for 5 min. The films were then rinsed with DI water, isopropanol, and acetone, and then dried in a glovebox. Thin layers of 8 nm MoO_x and 100 nm of Ag were then thermally evaporated through a shadow mask at ~10^{-6} Torr.

All-Polymer Solar Cell Characterization: Device *I–V* characteristics were measured under AM1.5G light (100 mW cm^{-2}) using the Xe arc lamp of a Spectra-Nova Class A solar simulator. The light intensity was calibrated using an NREL-certified monocrystalline Si diode coupled to a KG3 filter to bring spectral mismatch to unity. Four-point contact measurements were performed and electrical characterization was carried out with a Keithley 2400 unit. The area of all devices was 6 mm^2, and an aperture was used on top of cells during measurements. EQEs were characterized using an Oriel model QE-PV-SI instrument equipped with an NIST-certified Si diode. Monochromatic light was generated from an Oriel 300W lamp source.

DFT Calculations: Density functional theory (DFT) calculations were performed using the B3LYP functional[39] and the 6–31 G** basis set[40] as implemented in GAUSSIAN 03.[41]

Supporting Information

Supporting Information is available from the Wiley Online Library or from the author.

Acknowledgements

This research was supported as part of the ANSER Center, an Energy Frontier Research Center funded by the U.S. Department of Energy, Office of Science, and Office of Basic Energy Sciences under Award Number DE-SC0001059, by AFOSR (FA9550–08–1–0331), and by Polyera Corp. The authors thank the NSF-MRSEC program through the Northwestern University Materials Research Science and Engineering Center for characterization facilities (DMR-1121262) and Institute for Sustainability and Energy at Northwestern (ISEN) for partial equipment funding. H.H. thanks Chinese Academy of Sciences "100 Talents" program and the National Natural Science Foundation of China (51303180). Research at University of Malaga was supported by MINECO (CTQ2012–33733) and Junta de Andalucia (P09–4708). R.P.O. thanks MINECO for a Ramon Cajal research contract.

Received: September 17, 2013
Revised: November 10, 2013
Published online: January 16, 2014

[1] a) X. Guo, J. Quinn, Z. Chen, H. Usta, Y. Zheng, Y. Xia, J. Hennek, R. P. Ortiz, T. J. Marks, A. Facchetti, *J. Am. Chem. Soc.* **2013**, *135*, 1986–1996; b) N. Shin, J. Kang, L. J. Richter, V. M. Prabhu, R. J. Kline, D. A. Fischer, D. M. DeLongchamp, M. F. Toney, S. K. Satija, D. J. Gundlach, B. Purushothaman, J. Anthony, D. Y. Yoon, *Adv. Funct. Mater.* **2013**, *23*, 336–376; c) C. Wang, H. Dong, W. Hu, Y. Liu, D. Zhu, *Chem. Rev.* **2012**, *112*, 2208–2267; d) I. McCulloch, R. S. Ashraf, L. Biniek, H. Bronstein, C. Combe, J. E. Donaghey, D. I. James, C. B. Nielsen, B. C. Schroeder, W. Zhang, *Acc. Chem. Res.* **2012**, *45*, 714–722; e) H. T. Yi, M. M. Payne, J. E. Anthony, V. Podzorov, *Nat. Commun.* **2012**, *3*, 1–7; f) H. Kong, B. J. Jung, J. Sinha, H. E. Katz, *Chem. Mater.* **2012**, *24*, 2621–2623; g) H. Bronstein, Z. Chen, R. S. Ashraf, W. Zhang, J. Du, J. R. Durrant, P. Shakya Tuladhar, K. Song, S. E. Watkins, Y. Geerts, M. M. Wienk, R. A. J. Janssen, T. Anthopoulos, H. Sirringhaus, M. Heeney, I. McCulloch, *J. Am. Chem. Soc.* **2011**, *133*, 3272–3275; h) G. Giri, E. Verploegen, S. C. B. Mannsfeld, S. Atahan-Evrenk, D. H. Kim, S. Y. Lee, H. A. Becerril, A. Aspuru-Guzik, M. F. Toney, Z. Bao, *Nature*, **2011**, *480*, 504–508; i) I. Osaka, R. Zhang, G. Sauve, D.-M. Smilgies, T. Kowalewski, R. D. McCullough, *J. Am. Chem. Soc.* **2009**, *131*, 2521–2529.

[2] a) H. J. Son, L. Lu, W. Chen, T. Xu, T. Zheng, B. Carsten, J. Strzalka, S. B. Darling, L. X. Chen, L. Yu, *Adv. Mater.* **2013**, *25*, 838–843; b) A. Stuart, J. R. Tumbleston, H. Zhou, W. Li, S. Liu, H. Ade, W. You, *J. Am. Chem. Soc.* **2013**, *135*, 1806–1815; c) B.-G. Kim, X. Ma, C. Chen, Y. Le, E. Coir, H. Hashemi, Y. Aso, P. F. Green, J. Kieffer, J. Kim, *Adv. Funct. Mater.* **2013**, *23*, 439–445; d) G. Li, R. Zhu, Y. Yang, *Nat. Photonics* **2012**, *6*, 153–161; e) P. M. Beaujuge, J. M. J. Frechet, *J. Am. Chem. Soc.* **2011**, *133*, 20009–20029; f) C. Li, M. Liu, N. G. Pschirer, M. Baumgarten, K. Muellen, *Chem. Rev.* **2010**, *110*, 6817–6855; g) C. J. Brabec, S. Gowrisanker, J. J. M. Halls, D. Laird, S. Jia, S. P. Williams, *Adv. Mater.* **2010**, *22*, 3839–3856; h) Y.-J. Cheng, S.-H. Yang, C.-S. Hsu, *Chem. Rev.* **2009**, *109*, 5868–5923; i) S. Guenes, H. Neugebauer, N. S. Sariciftci, *Chem. Rev.* **2007**, *107*, 1324–1338.

[3] J. Roncali, *Macromol. Rapid. Commun.* **2007**, *28*, 1761–1775.

[4] J. Liu, R. Zhang, G. Sauve, T. Kowalewski, R. D. McCullough, *J. Am. Chem. Soc.* **2008**, *130*, 13167–13176.

[5] a) W. Wu, Y. Liu, D. Zhu, *Chem. Soc. Rev.* **2010**, *39*, 1489–1502; b) H. Usta, G. Lu, A. Facchetti, T. J. Marks, *J. Am. Chem. Soc.* **2006**, *128*, 9034–9035; c) H. Usta, C. Risko, Z. Wang, H. Huang, M. K. Deliomeroglu, A. Zhukhovitskiy, A. Facchetti, T. J. Marks, *J. Am. Chem. Soc.* **2009**, *131*, 5586–5608; d) H. H. Fong, V. A. Pozdin, A. Amassian, G. G. Malliaras, D. M. Smilgies, M. Q. He, S. Gasper, F. Zhang, M. Sorensen, *J. Am. Chem. Soc.* **2008**, *130*, 13202–13203; e) M. Q. He, J. F. Li, M. L. Sorensen, F. X. Zhang, R. R. Hancock, H. H. Fong, V. A. Pozdin, D. M. Smilgies, G. G. Malliaras, *J. Am. Chem. Soc.* **2009**, *131*, 11930–11938; f) X. Guo, R. P. Ortiz, Y. Zheng, Y. Hu, Y.-Y. Noh, K.-J. Baeg, A. Facchetti, T. J. Marks, *J. Am. Chem. Soc.* **2011**, *133*, 1405–1418; g) Y.-X. Xu, C.-C. Chueh, H.-L. Yip, F.-Z. Ding, Y.-X. Li, C.-Z. Li, X. Li, W.-C. Chen, K. Y. Jen Alex, *Adv. Mater.* **2012**, *24*, 6356–6361.

[6] a) J. Roncali, P. Blanchard, P. Frere, *J. Mater. Chem.* **2005**, *15*, 1589–1610; b) X. Guo, F. S. Kim, S. A. Jenekhe, M. D. Watson, *J. Am. Chem. Soc.* **2009**, *131*, 7206–7207; c) X. Guo, J. Quinn, Z. Chen, H. Usta, Y. Zheng, Y. Xia, J. W. Hennek, R. P. Ortiz, T. J. Marks, A. Facchetti, *J. Am. Chem. Soc.* **2013**, *135*, 1986–1996; d) X. Guo, R. P. Ortiz, Y. Zheng, M.-G. Kim, S. Zhang, Y. Hu, G. Lu, A. Facchetti, T. J. Marks, *J. Am. Chem. Soc.* **2011**, *133*, 13685–13697.

[7] J. Roncali, *Chem. Rev.* **1992**, *92*, 711–738.

[8] D. M. de Leeuw, M. M. J. Simenon, A. R. Brown, R. E. F. Einerhand, *Synth. Met.* **1997**, *87*, 53–59.

[9] F. S. Kim, X. Guo, M. D. Watson, S. A. Jenekhe, *Adv. Mater.* **2010**, *22*, 478.

[10] H. Huang, Z. Chen, R. P. Ortiz, C. Newman, H. Usta, S. Lou, J. Youn, Y.-Y. Noh, K.-J. Baeg, L. X. Chen, A. Facchetti, T. Marks, *J. Am. Chem. Soc.* **2012**, *134*, 10966–10973.

[11] H. Usta, A. Facchetti, T. J. Marks, *J. Am. Chem. Soc.* **2008**, *130*, 8580–8581.

[12] a) H. Yan, Z. Chen, Y. Zheng, C. Newman, J. R. Quinn, F. Dotz, M. Kastler, A. Facchetti, *Nature* **2009**, *457*, 679–686; b) Y. Liang, D. Feng, Y. Wu, S.-T. Tsai, G. Li, C. Ray, L. Yu, *J. Am. Chem. Soc.* **2009**, *131*, 7792–7799; c) Z. Chen, Y. Zheng, H. Yan, A. Facchetti, *J. Am. Chem. Soc.* **2009**, *131*, 8–9.

[13] J. Roncali, R. Garreau, A. Yassar, P. Marque, F. Garnier, M. Lemaire, *J. Phys. Chem.* **1987**, *91*, 6706–6714.

[14] a) F. Zhang, Y. Hu, T. Schuettfort, C.-a. Di, X. Gao, C. R. McNeill, L. Thomsen, S. C. B. Mannsfeld, W. Yuan, H. Sirringhaus, D. Zhu, *J. Am. Chem. Soc.* **2013**, *135*, 2338–2349; b) K. H. Kim, Z. Chi, M. J. Cho, J.-I. Jin, D. H. Choi, S. H. Paek, *Macromol. Symp.* **2007**, *249/250*, 1–7; c) S. H. Chen, Y. Zhu, S. A. Jenekhe, A. C. Su, S. A. Chen, *J. Phys. Chem. B* **2007**, *111*, 12345–12350; d) A. T. Yiu, P. M. Beaujuge, O. P. Lee, C. H. Woo, M. F. Toney, J. M. J. Frechet, *J. Am. Chem. Soc.* **2012**, *134*, 2180–2185.

[15] H. Huang, J. Youn, R. P. Ortiz, Y. Zheng, A. Facchetti, T. Marks, *Chem. Mater. 23*, 2185–2200.

[16] a) A. Facchetti, *Mater. Today* **2013**, *16*(4), 123–132; b) X. Guo, T. J. Marks, *Proc. SPIE* **2013**, *8622*, 86220K-1–10; c) X. Guo, N. Zhou, S. J. Lou, J. Smith, D. B. Tice, J. W. Hennek, R. P. Ortiz, J. T. L. Navarrete, S. Li, J. Strzalka, L. X. Chen, R. P. H. Chang, A. Facchetti, T. J. Marks, *Nat. Photonics* **2013**, *7*, 825–833; d) P. Sonar, J. Lim, F. Pui, K. Chan, *Energy Environ. Sci.* **2011**, *4*, 1558–1574.

[17] a) M. D. Irwin, D. B. Buchholz, A. W. Hains, R. P. H. Chang, T. J. Marks, *Proc. Natl. Acad. Sci. U. S. A.* **2008**, *105*, 2783–2787; b) S. C. Price, A. C. Stuart, L. Yang, H. Zhou, W. You, *J. Am. Chem. Soc.*, **2011**, *133*, 4625–4631; c) X. Guo, N. Zhou, S. J. Lou, J. W. Hennek, R. P. Ortiz, M. R. Butler, P.-L. T. Boudreault, J. Strzalka, P.-O. Morin, M. Leclerc, J. T. Lopez Navarrete, M. A. Ratner, L. X. Chen, R. P. H. Chang, A. Facchetti, T. J. Marks, *J. Am. Chem. Soc.* **2012**, *134*, 18427–18439; d) N. Zhou, X. Guo, R. P. Ortiz, S. Li, S. Zhang, R. P. H. Chang, A. Facchetti, T. J. Marks, *Adv. Mater.* **2012**, *24*, 2242–2248; e) C. E. Small, S. Chen, J. Subbiah, C. M. Amb, S.-W. Tsang, T.-H. Lai, J. R. Reynolds, F. So, *Nat. Photonics* **2012**, *6*, 115–120.

[18] a) C. Reese, M. E. Roberts, S. R. Parkin, Z. Bao, *Adv. Mater.* **2009**, *21*, 3678–3681; b) R. Schmidt, J. H. Oh, Y.-S. Sun, M. Deppisch, A.-M. Krause, K. Radacki, H. Braunschweig, M. Koenemann, P. Erk, Z. Bao, F. Wuerthner, *J. Am. Chem. Soc.* **2009**, *131*, 6215–6228.

[19] a) M. Schubert, D. Dolfen, J. Frisch, S. Roland, R. Steyrleuthner, B. Stiller, Z. Chen, U. Scherf, N. Koch, A. Facchetti, D. Neher, *Adv. Energy Mater.* **2012**, *2*, 369–380; b) M. L. Tang, S. C. B. Mannsfeld, Y.-S. Sun, H. A. Becerril, Z. Bao, *J. Am. Chem. Soc.* **2009**, *131*, 882–883; c) I. Osaka, T. Abe, S. Shinamura, E. Miyazaki, K. Takimiya, *J. Am. Chem. Soc.* **2010**, *132*, 5000–5001; d) E. Zhou, J. Cong, Q. Wei, K. Tajima, C. Yang, K. Hashimoto, *Angew. Chem. Inter. Ed.* **2011**, *50*, 2799–2803; e) S. Rajaram, R. Shivanna, S. Kandappa, K. S. Narayan, *J. Phys. Chem. Lett.* **2012**, *3*, 2405–2408; f) K. Nakabayashi, H. Mori, *Macromolecules* **2012**, *45*, 9618–9625; g) Y.-J. Hwang, G. Ren, N. Murari, S. Jenekhe, *Macromolecules* **2012**, *45*, 9056–9062.

[20] Y. Liang, Z. Xu, J. Xia, S.-T. Tsai, Y. Wu, G. Li, C. Ray, L. Yu, *Adv. Mater.* **2010**, *22*, E135–E138.

[21] S. R. Puniredd, A. Kiersnowski, G. Battagliarin, W. Zajaczkowski, W. W. H. Wong, N. Kirby, K. Mullen, W. Pisula, *J. Mater. Chem. C* **2013**, *1*, 2433.

[22] a) J. Zhang, D. Deng, C. He, Y.-J. He, M.-J. Zhang, Z.-G. Zhang, Z.-J. Zhang, Y.-F. Li, *Chem. Mater.* **2011**, *23*, 817–822; b) P. Sista, J. Hao, S. Elkassih, E. E. Sheina, M. C. Biewer, B. G. Janesko, M. C. Stefan, *J. Polym. Sci. A: Polym. Chem.* **2011**, *49*, 4172–4179; c) Y. He, Y. Zhou, G. Zhao, J. Min, X. Guo, B. Zhang, M. Zhang, J. Zhang, Y. Li, F. Zhang, O. Inganaes, *J. Polym. Sci. A: Polym. Chem.* **2010**, *48*, 1822–1829; d) H. Yan, Z. Chen, Y. Zheng, C. Newman, J. R. Quinn, F. Dotz, M. Kastler, A. Facchetti, *Nature* **2009**, *457*, 679–686.

[23] Y. Zhu, M. M. Alam, S. A. Jenekhe, *Macromolecules* **2002**, *35*, 9844–9846.

[24] a) M. Petersilka, U. J. Gossmann, E. K. U. Gross, *Phys. Rev. Lett.* **1996**, *76*, 1212–1215; b) C. Jamorski, M. E. Casida, D. R. Salahub, *J. Chem. Phys.* **1996**, *104*, 5134–5147; c) M. E. Casida, C. Jamorski, K. C. Casida, D. R. Salahub, *J. Chem. Phys.* **1998**, *108*, 4439–4449.

[25] I. Osaka, R. D. McCullough, *Acc. Chem. Res.* **2008**, *41*, 1202–1214.

[26] Y. Liang, D. Feng, Y. Wu, S.-T. Tsai, G. Li, C. Ray, L. Yu, *J. Am. Chem. Soc.* **2009**, *131*, 7792–7799.

[27] G. Sang, Y. Zou, Y. Huang, G. Zhao, Y. Yang, Y. Li, *Appl. Phys. Lett.* **2009**, *94*, 193302–193304.

[28] Y. Sun, C. J. Takacs, S. R. Cowan, J. H. Seo, X. Gong, A. Roy, A. Heeger, *Adv. Mater.* **2011**, *23*, 2226.

[29] a) M. C. R. Delgado, E.-G. Kim, D. A. d. S. Filho, J.-L. Brédas, *J. Am. Chem. Soc.* **2010**, *132*, 3375–3387; b) M. Malagoli, J. -L. Brédas, *Chem. Phys. Lett.* **2000**, *327*, 13–17.

[30] M. G. Debije, J. Piris, M. P. de Haas, J. M. Warman, Z. Tomović, C. D. Simpson, M. D. Watson, K. Müllen, *J. Am. Chem. Soc.* **2004**, *126*, 4641–4645.

[31] J. Zaumseil, H. Sirringhaus, *Chem. Rev.* **2007**, *107*, 1296–1323.

[32] a) R. P. Ortiz, H. Herrera, R. l. Blanco, H. Huang, A. Facchetti, T. J. Marks, Y. Zheng, J. L. Segura, *J. Am. Chem. Soc.* **2010**, *132*, 8440–8452; b) R. P. Ortiz, H. Herrera, C. Seoane, J. L. Segura, A. Facchetti, T. J. Marks, *Chemistry* **2012**, *18*, 532–543.

[33] a) K. Szendrei, D. Jarzab, Z. Chen, A. Facchetti, M. A. Loi, *J. Mater. Chem.* **2010**, *20*, 1317–1321; b) M. A. Loi, C. Rost-Bietsch, M. Murgia, S. Karg, W. Riess, M. Muccini, *Adv. Funct. Mat.* **2006**, *16*, 41–47; c) M. Shkunov, R. Simms, M. Heeney, S. Tierney, I. McCulloch, *Adv. Mater.* **2005**, *17*, 2608–2612.

[34] J. R. Moore, S. Albert-Seifried, A. Rao, S. Massip, B. Watts, D. J. Morgan, R. H. Friend, C. R. McNeill, H. Sirringhaus, *Adv. Energy Mater.* **2011**, *1*, 230–240.

[35] a) Y. Tang, C. McNeil, *J. Polym. Sci., Part B: Polym. Phys.* **2013**, *51*, 403–409; b) E. Zhou, J. Cong, M. Zhao, L. Zhang, K. Hashimoto, K. Tajima, *Chem. Commun.* **2012**, *42*, 5283–5285.

[36] M. M. Mandoc, W. Veurman, L. J. A. Koster, B. de Boer, P. W. M. Blom, *Adv. Funct. Mat.* **2007**, *17*, 2167–2173.

[37] P.-T. Wu, H. Xin, F. S. Kim, G. Ren, S. Jenekhe, *Macromolecules*, **2009**, *42*, 8817–8826.

[38] a) M. D. Clark, M. L. Jespersen, R. J. Patel, B. J. Leever, *ACS Appl. Mater. Interfaces* **2013**, *5*, 4799–4807; b) X. Guo, N. Zhou, S. J. Lou, J. Smith, D. B. Tice, J. W. Hennek, R. P. Ortiz, J. T. L. Navarrete, S. Li, J. Strzalka, L. X. Chen, R. P. H. Chang, A. Facchetti, T. J. Marks, *Nat. Photonics* **2013**, *7*, 825.

[39] A. D. Becke, *J. Chem. Phys.* **1993**, *98*, 1372–1377.

[40] M. M. Francl, W. J. Pietro, W. J. Hehre, J. S. Binkley, M. S. Gordon, D. J. DeFrees, J. A. Pople, *J. Chem. Phys.* **1982**, *77*, 3654–3665.

[41] M. J. Frisch, Gaussian 03, Revision B.04 ed., Pittsburgh, PA, **2003**.